

Planetary Scale Analysis of the Morphology of River Channels and Channel Belt Deposits*

Björn Nyberg^{1,2*}, Gijs Henstra³, Rob Gawthorpe¹, Rodmar Ravnås³, Juha Ahokas³

Department of Earth Sciences, University of Bergen, Allegaten 41, 5020, Bergen, Norway.¹

Bjerknes Centre for Climate Research, Allegaten 70, 5020, Bergen, Norway.²

AkerBP ASA, Oksenøyveien 10, 1366 Lysaker, Norway.³

Abstract

The morphology of a river and its channel belt is in part the product of ecological, hydrological and tectonic processes shaping the terrestrial landscape. River morphology is critical for understanding their physical evolution through time, and in predicting the future behavior of rivers and floods. To date, there is no global-scale, quantitative study of the morphology of rivers and their channel belt deposits. Based on a pattern recognition algorithm, we can calculate that the global surface area of channel belts, at an approximate 1 km resolution, is estimated at $30.5 \times 10^5 \text{ km}^2$, seven times larger than the extent of river channels. We find that 52% of river channels have a more braided planform morphology with the remaining 48% being more meandering. The new global river morphology (GRM) map and datasets allows new ways to study river morphology and to improve analysis of flood mitigation, freshwater resources management, and ecosystem accounting.

*This paper is a non-peer reviewed preprint uploaded to EarthArXiv. The manuscript is currently under review at *Nature Communications*.

Main

Rivers are widely recognized as an essential part for life on Earth supporting ecosystems^{1,2}, influencing our climate³ and providing freshwater resources⁴. Rivers can also be destructive with an estimated 1 billion people living in flood-prone regions causing an annual projected 1,250 billion Euros in socio-economic damage by the year 2050⁵. While hydrological modeling has shown the historical and predicted extent of rivers and their floods⁵⁻⁷, the morphology of a river is not considered in these studies, yet river morphology controls the long-term evolution and future behavior of a river⁸. With floods expected to increase in both intensity and frequency during this century due to climate change⁵, knowledge on the distribution of current rivers, their extent and morphology is vital to best conserve riverine ecosystems and to improve existing flood adaptation strategies⁸.

Numerous classification schemes have been proposed to characterize rivers based on aspects such as their morphology, hydrology, mode of sediment transport and/or their deposits^{2,8-12}. The most recognized is based on a simple plan-view morphology of the channel belt that distinguishes between meandering, braided, straight or sinuous rivers^{12,13}. The channel belt represents the sedimentary deposits created by the river as it migrates laterally to build and erode land over time and is typically composed of three main components: the river channel(s), the active channel belt(s), and the abandoned “paleo” channel belt(s) (Figure 1). Here we define the channel belt morphology by the planform character of the river channel and its deposits.

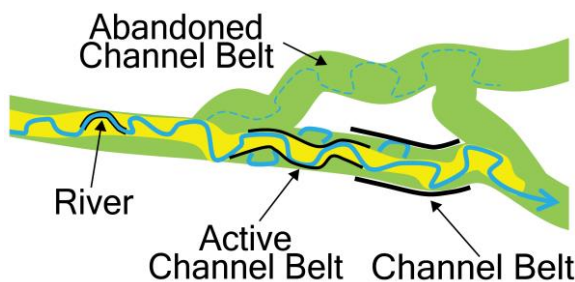


Figure 1 Channel Belt Terminology – Schematic illustration of the channel belt that includes the channel belt, the active channel belt and the river. The channel belt represents all features associated with the river and its lateral migration including previously abandoned channel belts. The active channel belt refers to the actively migrating river extent over the past 37-years of available Landsat imagery. The river refers to the extent of the river waterbody based on an annual averaged water discharge.

Meandering river systems show river channels that meander to create point-bar accretions, and overbank deposits with oxbow lakes on its channel belt. Braided river systems are defined by multiple river channels (thalwegs) separating exposed alluvial mid-channel bars and lateral bar accretions¹². Lastly, rivers may be straight or sinuous (sinuosity < 1.25¹²), typically representing entrenched river channels with a stable planform character. In reality, river systems are more likely on a spectrum between these end-member classifications. Furthermore, each river channel may be single- or multi- threaded (anabranching), the latter of which is characterized by multiple river channels or channel belts separated by stable vegetated islands that may persist for several decades¹³. To date, there is no existing planetary scale analysis on the geomorphology of rivers, or the extent of their channel belt deposits.

In recent years, integration of data from satellite missions has allowed compilation of detailed high-resolution planetary scale studies of landcover and water surface change¹⁴⁻¹⁷. Yet, previous planetary scale classifications of river systems are either limited to classifications of drainage networks^{2,18}, descriptions of river morphologies based on high-resolution imagery^{19,20}, or measurements of the river geometry based manually interpreted channel belts from a relatively small selection of river systems²¹. Only recently have Allen and Pavelsky³ calculated the global surface area of rivers greater than 30 m² covers an estimated 468,000 km² or 0.35% of Earth's non-glaciated land surface. This work has also been expanded to show the historical change in river widths over the past 37 years based on water surface change detection²². However, these studies do not map the extent of the channel belt deposits or the

morphology of river systems, both of which are important for understanding the behavior of rivers and the different ecosystems within river channels and its channel belt². A major challenge in mapping the channel belt is that it is formed across a range of different climates, vegetation coverage and lithologies that are difficult to constrain with traditional pixel-based classification techniques.

Here we build the first global river morphology (GRM) map and dataset to characterize the extent and morphology of river channels and channel belts based on 30 m resolution Landsat 8 imagery. By implementing pattern recognition (Figure 2) trained to 370 manually interpreted river systems across a range of different climates and geographical regions, we can predict the morphology and extent of channel belts to a 94% accuracy (see Methods; Extended Figures 1 and 2). We use a three-class meandering, braided and background classification model applied to a cloud- and snow-free Landsat 8 composite image for the year 2020 consisting of 151,723 image scenes. While we recognize the complexity of river systems, the meandering and braided river classification is a simplest distinguishing planform character of river systems^{9,11,13}, and our approach quantifies the probability (0 to 100%) for each category to occur at any given location, providing a continuum range between the end-members rather than one fixed class as used in alternative approaches^{19,20}. Thus, the GRM model offers a valuable new resource and method towards classifying river morphology that shows the variability that exists in rivers and their channel belts that can aid in ecosystem accounting, freshwater resource management, and flood mitigation studies.

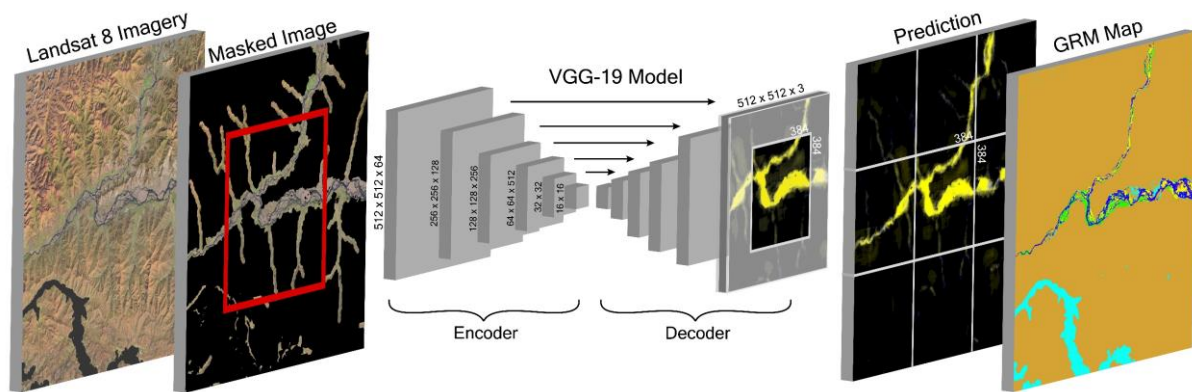


Figure 2 Global River Morphology Model – The GRM model is based on a VGG-19³⁹ machine learning algorithm for pattern recognition of channel belt extent and morphology. The algorithm uses 512x512 pixel tiles of Landsat 8 images masked for non-riverine regions using a series of convolutions and upscaling functions to simplify the prediction for a 3-class prediction of braided, meandering or background. The resulting channel belt prediction is used to describe the distribution of fluvial and lacustrine environments. See methods for more detail.

Global River and Channel Belt Morphology Map

The observable extent of channel belts covers a surface area of $30.5 \times 10^5 \text{ km}^2$ (Figure 3; see data availability section for interactive map), nearly 7 times larger than the previously documented extent of rivers³. This value is based on the reported 50% confidence interval of the GRM model at an approximately 1 km resolution (see methods for validation). Globally, 37% of channel belts are in Asia ($11.4 \times 10^5 \text{ km}^2$), followed by 23% in South America ($7.4 \times 10^5 \text{ km}^2$), 14% in North America ($4.3 \times 10^5 \text{ km}^2$), 12% in Africa ($3.6 \times 10^5 \text{ km}^2$), 7% in Europe ($2.0 \times 10^5 \text{ km}^2$) and another 6% in Oceania ($1.8 \times 10^5 \text{ km}^2$; Extended Table 1).

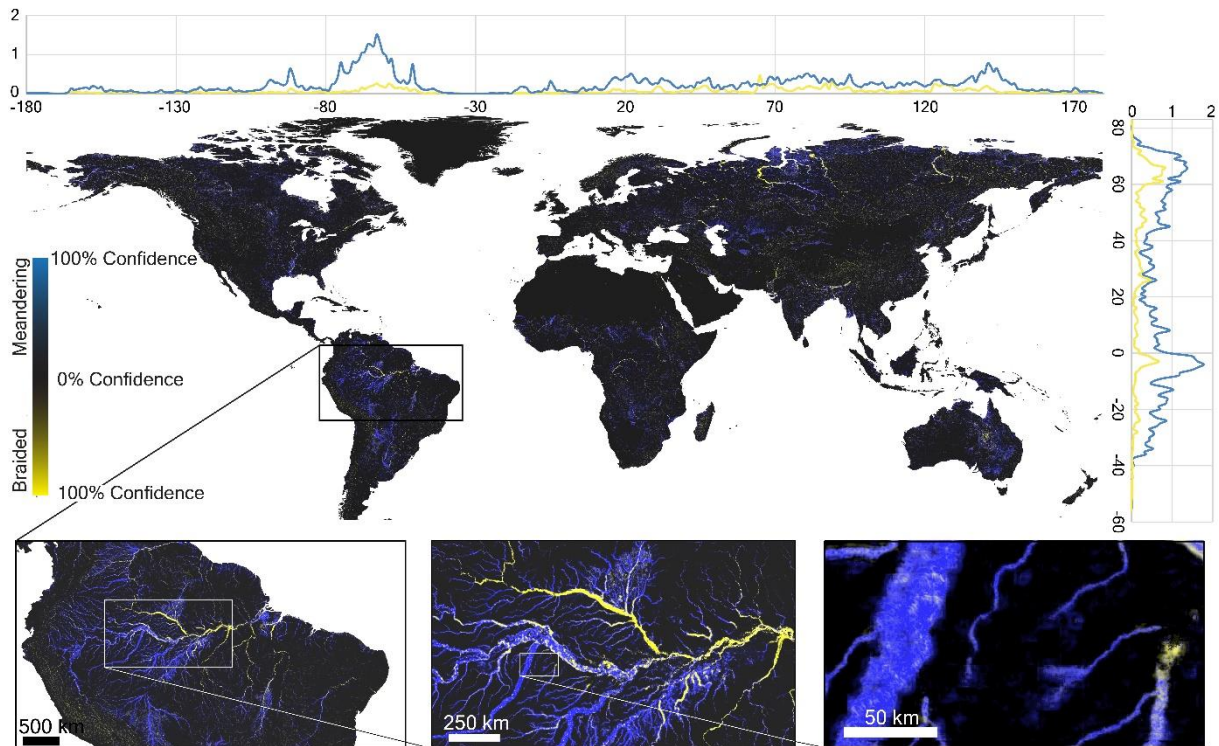


Figure 3 Planetary Scale Analysis of River Morphology – Map shows the predicted extent of channel belts and morphology. Latitudinal and longitudinal plots show the proportion of meandering and braided channel belts as a percentage of the total. See data availability section for a detailed interactive map and publicly available dataset.

Within the defined channel belt extent, the highest estimated probability shows that 77% of channel belts are defined by a more meandering planform character with the remaining 23% being more braided in (Extended Table 1). Braided and bifurcating rivers tend to dominate the larger rivers found in high latitude areas such as Siberia and northwestern Canada and Alaska, as well as in equatorial and temperate regions of the Amazon, Congo, Bangladesh, India, and Pakistan (Extended Figure 3). Meandering rivers are frequently more common across the entire river catchment. Channel belts classified as meandering tend to dominate Africa, North America, South America, and Oceania ranging between 78 and 86% with a lower percentage found in Europe and Asia (68 and 71% of the total surface area, respectively; Extended Table 1).

Riverine and Lacustrine Environments

Based on the known extent of the predicted channel belt, we are further able to produce a new global classification of riverine and lacustrine / wetland waterbodies for the year 2020 (Figure 4, Extended Figure 4). Here we classify elements within the channel belt into; 1) active river channels, 2) smaller streams and oxbow lakes, 3) the active channel belt, and 4) the abandoned “paleo” channel belt. This is achieved by classifying active river channels as those waterbodies within a channel belt that are connected over at least a ~4.5 km distance while the remaining waterbodies are defined as likely smaller streams or oxbow lakes. We define the active channel belt as the maximum seasonal migration of the active river channel based on the archive of 37-years of Landsat imagery. The remaining area without an active river channel or recent channel migration are defined as the abandoned channel belt. Finally, waterbodies that are defined outside the channel belt are classified as either lakes or wetlands (see methods for further detail and validation).

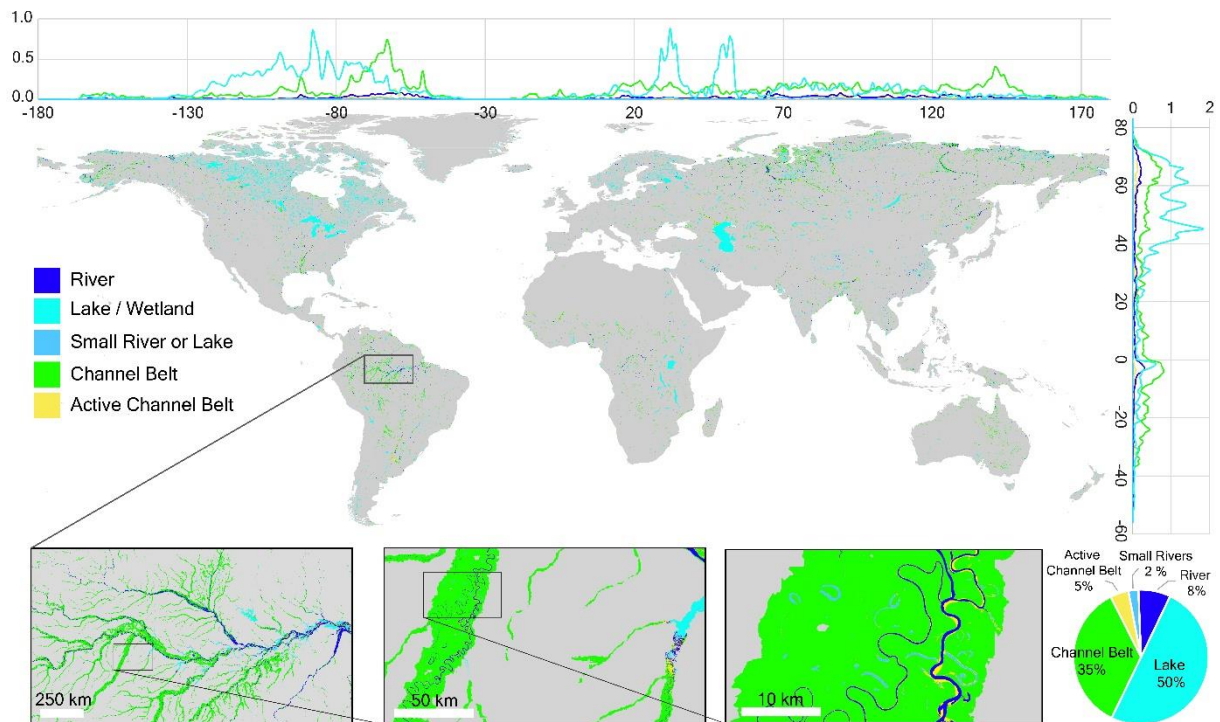


Figure 4 Planetary Scale Analysis of Riverine and Lacustrine Environments - Map showing the distribution of rivers, lakes/wetlands, smaller rivers or lakes, channel belt and the active channel belt. Latitudinal and longitudinal plots show the proportion of riverine and lacustrine environments as a percentage of the total. See data availability section for a detailed interactive map and publicly available dataset.

The results show that the observable extent of channel belts (i.e. the river and its sedimentary deposits) covers a surface area of $30.5 \times 10^5 \text{ km}^2$, which is similar to the extent of lakes and wetlands at $30.6 \times 10^5 \text{ km}^2$. The distribution of environments shows that lakes and wetlands are most prevalent in high latitude regions whereas the channel belt environment becomes dominant in mid and low latitude regions (Figure 4, see data availability section for interactive map). Within channel belts, $22.7 \times 10^5 \text{ km}^2$ (71%) of the area are occupied by abandoned channel belts that once had an active river channel, but currently only show channel belt deposits. $2.70 \times 10^5 \text{ km}^2$ (9%) represent the 37-years of active channel belt migration since acquisitions of Landsat imagery began. Another $4.72 \times 10^5 \text{ km}^2$ (15%) are classified as river channels and the remaining $1.46 \times 10^5 \text{ km}^2$ (5%) are either smaller rivers/streams or oxbow lakes (Figure 1, Extended Table 1; see methods). The distribution of channel belt environments is highlighted in Figure 4, showing the dominance of the abandoned channel belts, particularly along ephemeral river systems, of for example, Australia and central Asia. Active channel belts are mostly associated with meandering rivers of equatorial regions as well as the larger braided river systems of the northern latitude regions. Whereas the present-day global surface area of channel belts has a dominantly meandering morphology (77%; Figure 3), the present-day global surface area of the river channels is shown to be more braided at 52% (Extended Table 1).

Controls on River Morphology

The hydrological, physio-climatic and tectonic conditions of the river channel by surface area are summarized in Figure 5 (see Methods). Rivers with medium or lower long-term averaged water discharge rivers ($<1000 \text{ m}^3 \text{ s}^{-1}$) represent approximately two-thirds of river channels by surface area. Another third of river channels are characterized by a high or very high ($>1000 \text{ m}^3 \text{ s}^{-1}$) water discharge. In terms of morphology, very low, as well as high and very high-water discharge rivers are commonly braided at 56, 58 and 75%, respectively. In contrast, the global surface area of river channels with a low and medium water discharged are only 40% braided (Figure 5A).

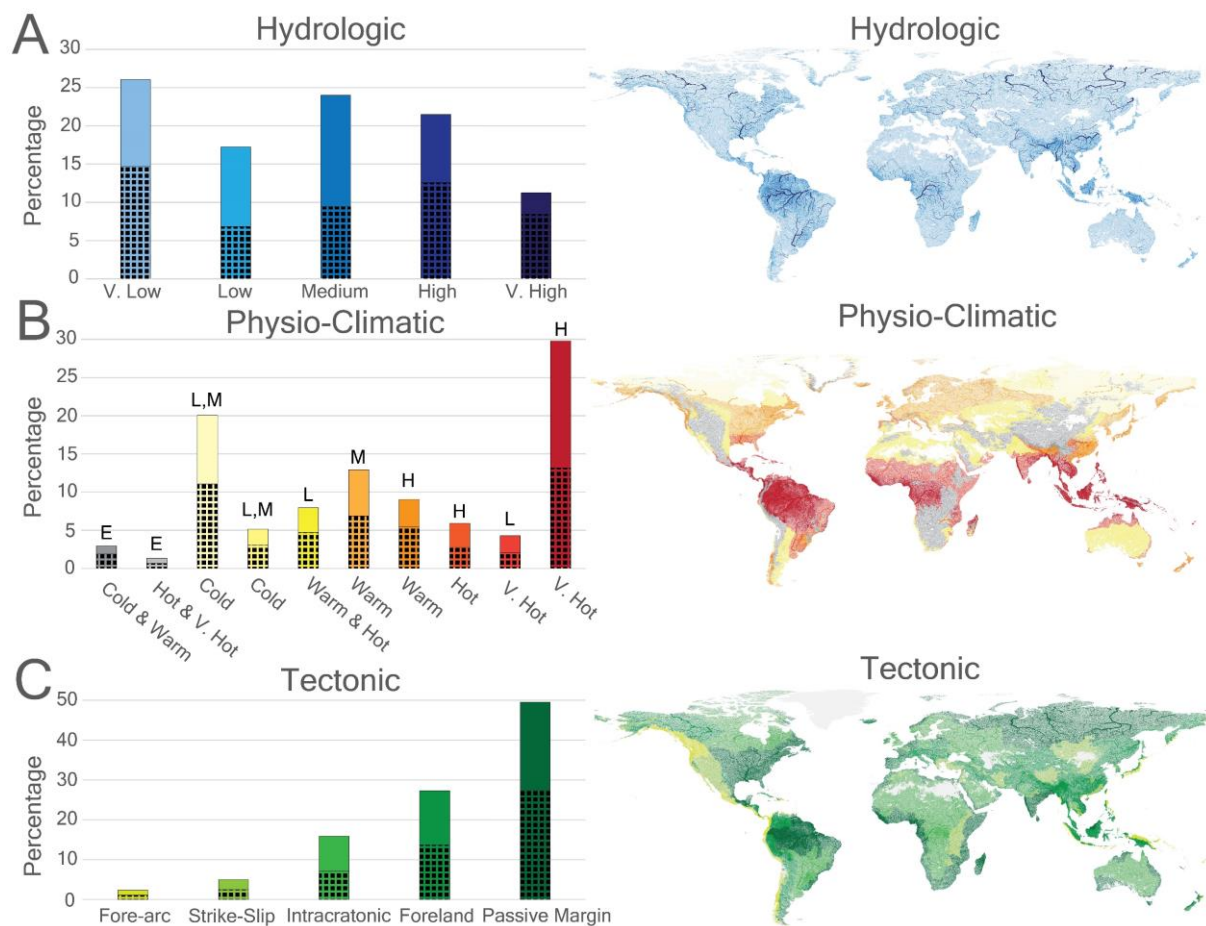


Figure 5 Global River Morphology Distribution and Controls – The hydrological (A), physio-climatic (B) and tectonic (C) distribution and controls on rivers as a percentage of river surface area visualized based on river reaches². The shaded region of each column shows the proportion of the total surface area of river channels defined as braided. Long-term averaged monthly river discharge is defined by Ouellet Dallaire et al.,² as very low ($0.1 - 10 \text{ m}^3 \text{ s}^{-1}$), low ($10 - 100 \text{ m}^3 \text{ s}^{-1}$), medium ($100 - 1000 \text{ m}^3 \text{ s}^{-1}$), high ($1000 - 10000 \text{ m}^3 \text{ s}^{-1}$) and very high ($> 10000 \text{ m}^3 \text{ s}^{-1}$). Physio-climatic conditions are defined by Ouellet Dallaire et al.,² based on three variables of temperature, climate moisture index (CMI; precipitation/potential evapotranspiration) and elevation. Categories show cold ($< -20 \text{ }^\circ\text{C}$), warm ($-20 - 5 \text{ }^\circ\text{C}$), hot ($5 - 20 \text{ }^\circ\text{C}$) or very hot ($> 20 \text{ }^\circ\text{C}$) long-term averaged minimum air temperature and a low (L; < 0.4 CMI), medium (M; $-0.4 - 0.125$ CMI), high (H; > 0.125 CMI) moisture index or a high (E; > 750 m) elevation. Tectonic regimes are defined by Nyberg et al., and include fore-arc, strike-slip (including extensional), intracratonic, foreland and passive margin settings.

Nearly 30% of river channels are associated with very hot ($> 20 \text{ }^\circ\text{C}$), high moisture (> 0.125 CMI) physio-climatic conditions in equatorial regions. River channels in these regions are slightly more meandering (56%; Figure 5B). Cold ($< 20 \text{ }^\circ\text{C}$), low and medium moisture ($< 0.4 - 0.125$ CMI) regions also contribute a significant 20% of the total surface area of river channels and are 55% braided in contrast to equatorial climates. Braided rivers are dominant in warm and hot ($-20 - 20 \text{ }^\circ\text{C}$) low (< 0.4 CMI) moisture regions, warm ($-20 - 5 \text{ }^\circ\text{C}$) and medium ($0.4 - 0.125$ CMI) moisture regions as well as cold and warm ($< 20 - 5 \text{ }^\circ\text{C}$) high elevation (> 750 m) regions at 60%, 60% and 65%, respectively.

When viewed by tectonic settings, 50% of river channels occur in passive margins, followed by foreland (27%) and intracratonic settings (16%) (Figure 5C). Extensional/strike-slip and forearc settings combined define the remaining 7% of river channels. This distribution of river channels is similar to the distribution of the tectonic regions globally²³. By morphology, we see that the proportion of braided to meandering river channels is relatively equal throughout the different tectonic regimes with intracratonic settings the most meandering at 56% and passive margins the most braided at 56%.

Broader Implications of GRM Model and Limitations

Existing methods to classify river morphology are based on manual interpretations^{20,24} or geometrical measurements of the river channel^{12,21} that are subjective, do not measure the gradual morphological change in rivers, and are impractical to apply at a global scale. As a result, river morphology is not captured in any existing global landcover, landuse, water surface area change maps^{15–17,25} or in traditional river network datasets representing rivers as simple lines of flow direction^{2,18,26}. The new GRM model highlights recent advances in pattern recognition to provide an objective and quantitative method to classifying river system extent and morphology. The model captures the range between end-member types comparable to typical measurements of the river channel geometry such as a braiding index or sinuosity as illustrated in Figure 6 for the Rio Bermejo in Argentina. While the current version of the GRM model do not encompass all river morphology classifications^{8,9,11,12,27}, the dataset provides a foundation to further constrain river types. Global lithological maps²⁸, digital elevation models²⁹, water surface change maps¹⁵ and the new riverine and lacustrine dataset of the current study (Figure 3) may further aid in river classifications for a specific study or objective.

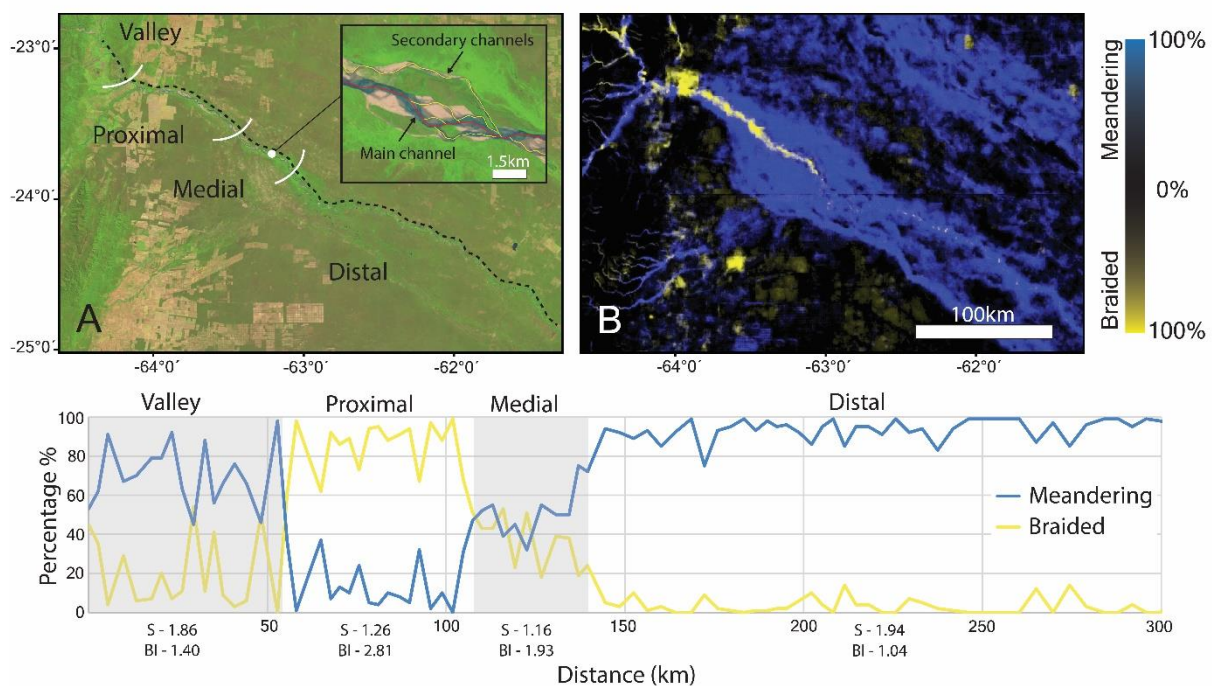


Figure 6 Example River Morphology Profile – A) Shows the original 2020 Landsat 8 imagery of the Rio Bermejo in Argentina. The dotted line is the profile used to sample the morphology of the active river channel every 5 km's for the plot shown below. B) Shows the resulting prediction from GRM model indicating the gradual braided to meandering trend common in many distributive fluvial systems^{19,20}. S refers to the sinuosity of the river channel (main channel length divided by the shortest valley path). BI is the braiding index defined as the total sum length of channels divided by the main channel length.

The new GRM model offer a wealth of new datasets to explore the impact of river morphology on flooding, ecosystems, climate, and water resource management. For instance, braided rivers are recognized to flood more frequently than meandering rivers^{1,8,12}. This is particularly true of monsoonal controlled braided river systems; for example, the Ganges/Brahmaputra, that experience annual flooding events³⁰. Meandering river systems have more stable river banks⁸, which may lead to more catastrophic flood events due to levee failures³¹. In comparison, anabranching systems, the rivers may dissipate flood energy more efficiently in its multiple river channels during high discharge events³². Knowledge of the extent and deposits within a channel belt is also important to understand the pathways taken as rivers avulse and may rejoin with previously abandoned channels. Furthermore, as a river evolves, changes in river morphology will also pose new flood risks¹ that are currently not

considered in future flood risk assessments⁵⁻⁷. The GRM model and dataset provide data to distinguish these different river morphologies and thus aid in assessment of flood risk.

The GRM dataset also builds on previous efforts to create a baseline study of current riverine state for ecosystem accounting to measure the impact of climate change on the environment². By incorporating observed river morphology to hydrological and climatological observations (Figure 5A), we can relate the behavior of river systems supporting different ecosystems. The extent of the river and its channel belt is also an important measure on the spatial impact of river systems on ecosystems which is not achieved by hydrological models^{2,26} alone. The changing surface area of rivers and lakes, and their deposits, are important to constrain biogeochemical fluxes of CO₂ and methane in inland waters^{3,33-35}. River morphology as a proxy for water discharge, sediment turbidity and sedimentation^{1,12} that in turn control outgassing into the atmosphere, carbon burial through sedimentation and carbon capture by photosynthesis, are a significant contribution to greenhouse emissions but not fully understood³⁴. Furthermore, changing surface water levels of rivers and lakes is important for improved water resource management and to map groundwater recharge⁴.

As with any model, the accuracy of the prediction depends on the reliability of the data inputs. Inherently, the model is limited by the 30 m Landsat imagery resolution split into roughly 512x512 pixel (~15 km²) tiles needed for the ML computations at a planetary scale (Figure 1; see Methods). A consequence is that the model may fail to recognize either the small- (< 150 m) or large-scale (>15 km) internal features within a channel belt that define a river's morphology or extent. This may lead to under- or over-estimations at the boundaries of the tiled images. Despite these limitations, our results suggest the GRM model compares well to the previously described geomorphology of river systems at a roughly 1 km scale resolution (see Methods). Whereas a larger training dataset would likely improve the resulting global classification, manually collecting large amounts of training data is time-consuming and inefficient. Here the relatively small training database of 370 river systems has allowed for the creation of a well-constrained image dataset suitable for the machine algorithm to learn. The resulting accuracy versus time-efficiency for analyzing remotely sensed imagery at a planetary scale shows the potential to apply similar methods to map the range of different sedimentary and other environments.

Methods

Training Data

A cloud and snow-free 2020 composite Landsat 8 imagery consisting of 151,723 scenes was created in the Google Earth Engine¹⁴. We manually interpret the Landsat imagery at 790 localities (Extended Figure 1) by overlaying each image with polygon interpretations that show the extent of the river and its channel belt as either meandering or braided at a 1:100,000 to 1:500,000 scale based on expert opinion. The interpreted polygons were then converted to an image mask at the same 30 m Landsat image resolution with any non-interpreted region defined as a background value (Extended Figure 2). Out of the 790 localities, 370 are riverine examples with an interpreted area ranging in size between 15 km² and 80 km² with channel belt widths that range between ~500 m to 30 km (e.g., Ob River). An additional 420 localities of non-riverine regions were selected covering a range of different climates, vegetation and landcovers. The location of the training images is randomly selected on the Earth's surface using several iterations to optimize the accuracy versus computational needs of the algorithm. In total, we collected a database containing 1090 images at a 512x512 tiled resolution of both riverine and non-riverine examples for training.

The Landsat 8 composite image averaging the pixel values gathered over the year likely represents a mean annual water discharge. While this is a source of uncertainty, a lack of data on months of low water discharge in global river systems prevents a more targeted image selection approach as noted in previous studies³. However, this issue is mitigated based on the pattern recognition approach classifying not only the river, but also its channel belt deposits as confirmed by the validation results (see Validation, Accuracy and Comparison section).

Data Augmentation

To further increase the number of images, we extract both 2016 and 2020 Landsat-8 imagery to increase the total number of scenes to 308,253 scenes and thus also increase the training dataset to 2180 images. The assumption is that both the spectral signatures and river morphology will be different for each year for the machine to learn. We limit this approach to two years to prevent overfitting the model and to reduce the computational requirements for the machine learning algorithm. In addition, we apply a series of common data augmentation techniques³⁶ to the images by randomly cropping between 70 and 100% of the original image, rotation between 90 and 360 degrees, and randomly flipping the resulting image. Given the scale invariance of river systems, the subsequent cropping, rotation and flipping augmentations will respect the morphology of the river systems while helping the model predict at different scales.

Planetary Scale Landsat-8 Imagery Processing

To reduce the number of images required to confidently identify river morphologies from non-riverine features, we implement a targeted image classification approach by masking the original Landsat 8 imagery for non-riverine regions (Figure 2). We remove Landsat imagery pixels that contain a mean slope greater than 2 degrees within a 270 m window (or approximately 3 pixels) based on the 90 m resolution MERIT Digital Elevation Model²⁹. Mountainous rivers in confined valleys were included by adding a 300 m radius (or ~10x Landsat imagery resolution) around river network lines with an upstream area larger than 50 km² and a water discharge greater than 0.1m³/s based on the free flowing rivers dataset¹⁸.

In addition, oceans identified by the Global Shoreline Vector³⁷ and previously defined lakes³⁸ greater than 10 km² were masked. This ensured that large waterbodies greater than the 512x512 (~15 km²) tiled resolution used in the machine learning predictions were correctly identified (Figure 2). Combined, these steps significantly reduced the number of training images required to identify the bounds of river channel belts in both mountainous and lowland regions. Finally, we only consider a false color RGB image using bands 6,5 and 4 of the Landsat 8 imagery to reduce the number of required input parameters and to be suitable for pre-trained machine learning models.

Machine Learning Model

The machine learning model was built in Tensorflow/Keras from a pretrained VGG-19 model³⁹ on the ImageNet dataset⁴⁰ with a custom decoder involving a series of 5 upscaling, convolutions and ReLU activation functions (Figure 2). The model was run with a batch size of 32 for 28 epochs based on a 3 run early stopping procedure on the reported validation accuracy. The 2180 images in our dataset are split into a training dataset for learning and validation dataset to test using a 70:30 ratio, respectively. Each epoch is refined based on an Adam optimizer and loss measured by a sparse categorical cross entropy. The model was trained on the Google Cloud AI platform using a n1 high-memory machine containing 64 virtual CPUs and 416GB of memory. The resulting model contains 21,353,943 parameters representing the internal variables of the machine learning algorithm (e.g., convolutions) used to objectively classify the Landsat imagery (Figure 2). Each parameter is created and assessed by the machine learning algorithm itself to design the best model based on the available training and validation dataset.

To apply the model, the algorithm requires a 512x512 image input and creates a 512x512 image prediction containing 3 layers of probability (0 to 100%), one for each meandering, braided and background category. To limit potential edge effects in the resulting prediction, we export the Landsat imagery for Tensorflow as a series of 512x512 tiles with a 128 pixel overlap to keep the central 384x384 pixels for the resulting output (Figure 2). To process the vast amount of data, we further split the data into 5064 2-degree tiles each with its own 0.1 degree overlap and run the model on five virtual machines on the Google Cloud Platform. By combining the tiled predictions, we can produce a seamless map of global river morphology prediction for the planet (see data availability section).

Riverine and lacustrine sedimentary map

The riverine and lacustrine map defines the channel belt, active channel belt, rivers, smaller rivers or lakes within the channel belt and lakes/wetlands. The extent of the entire channel belt is classified based on the 50% confidence boundary of the GRM model. The active channel belt is derived as the extent of at least 2 years of seasonal (>1 month) water occurrence over the past 37-years of available observations based on the Global Surface Water Map v1.3¹⁵. For the average waterbody extent of 2020, we use the modified normalized difference water index (MNDWI) in equation 1 with a 0.6 index threshold on a 2020 Landsat 8 composite following the same established procedure as many previous studies^{3,15}.

$$\text{MNDWI} = \frac{\text{green} - \text{SWIR}}{\text{green} + \text{SWIR}} \text{ (eq 1)}$$

where green is the green band and SWIR is the shortwave infrared band. Large bodies of water greater than 150 pixels connected within a 3x3 rectangular search window and at least a 10% channel belt confidence are assigned a river classification. Smaller bodies of water with an area less than 150 pixels within the channel belt are assigned as smaller rivers or lakes. This class represents smaller rivers that are typically disconnected at the 30 m Landsat resolution or smaller oxbow lakes that are a part of the channel belt environment. Finally, lakes and wetlands are defined as those permanent waterbodies with an area greater than 4 pixels that lie outside the defined channel belt environment and within 100 m from the coastline. This additional threshold was chosen to remove small clusters of pixel classifications that are difficult to identify as a waterbody based on Landsat imagery resolution.

River Morphology Controls

To constrain controls on river morphology, we combine the GRM map in our study with existing data on hydrologic, physio-climatic² and tectonic²³ descriptions (Figure 5). Given that the hydrological and physio-climatic descriptions of the GloRiC dataset² describe only the river reach, we expand that information to river extent by summarizing the information within sub-catchments of the HydroSHEDS level 12 product²⁶. The maximum river discharge and largest sum of river reach length by climate within each sub-catchment are assigned a pixel classification that is subsequently related to the surface area of the GRM product. For the tectonic classification, the catchment delineations of the GTSC dataset²³ are overlain on the GRM map for analysis.

Validation, Accuracy and Comparison

The machine learning classification of the extent and morphology of the channel belt shows a 96% accuracy to the training dataset and a 94% accuracy to the validation dataset with a loss of 0.13 and 0.15, respectively. Compared to the 415 manually described river morphologies by Hartley et al.¹⁹, 170 were below the resolution of the GRM model and excluded from comparison. Of the remaining 245 examples, the current GRM model achieves an 84% accuracy (Figure 7A). Another 10% of the locations were partially correct capturing one aspect of the river morphology while only 6% were incorrect. The channel belt width of the 170 excluded examples range between 10 m and 1300 m with a mean of 167 m (+/- 197m) and a 95% confidence interval at 623 m. Hence, while the resolution of the Landsat imagery is defined at 30 m, several pixels are required to identify the morphology of channel belts, thus lowering the resulting resolution of the GRM model to approximately 1 km.

The current GRM model shows a river surface area of $4.72 \times 10^5 \text{ km}^2$ (Extended Table 1) compared to the previously reported $4.7 \times 10^5 \text{ km}^2$ of Allen and Pavelsky³. Spatially, the discrepancy in river surface area is shown to be higher in high latitude regions and lower in mountainous regions (Figure 7B). This is likely since the river channel belt is less distinct in these regions and that the current study is based on an averaged river water discharge compared to a high-water discharge river surface area of the previous study. In total, the GRM model captures 91% of the river delineations by Allen and Pavelsky³ within the extent of the channel belt predictions.

Compared to the previously reported extent of lakes³⁸, the current study shows roughly a 4% larger surface area at $30.6 \times 10^5 \text{ km}^2$ (Extended Table 1). The most significant increase in lake surface area occurs along coastal wetlands and ephemeral salt lakes in South America, India and the Arctic that were not considered in the previous classification (Figure 7C). In addition, lake levels have increased in the Himalayas due to reported increase in glacial melting⁴¹. A decrease is most prominent in central Asia and Australia associated with water loss of the past three decades due to climate change and excess water demand¹⁵. An underestimation of lake extent in the Canadian shield and Scandinavia is likely a result in the overestimation of the channel belt extent used to define lakes in the current study. Overall, the new riverine and lacustrine map show a good correlation at the global scale with less than 1% difference in pixels per km^2 (Figure 7).

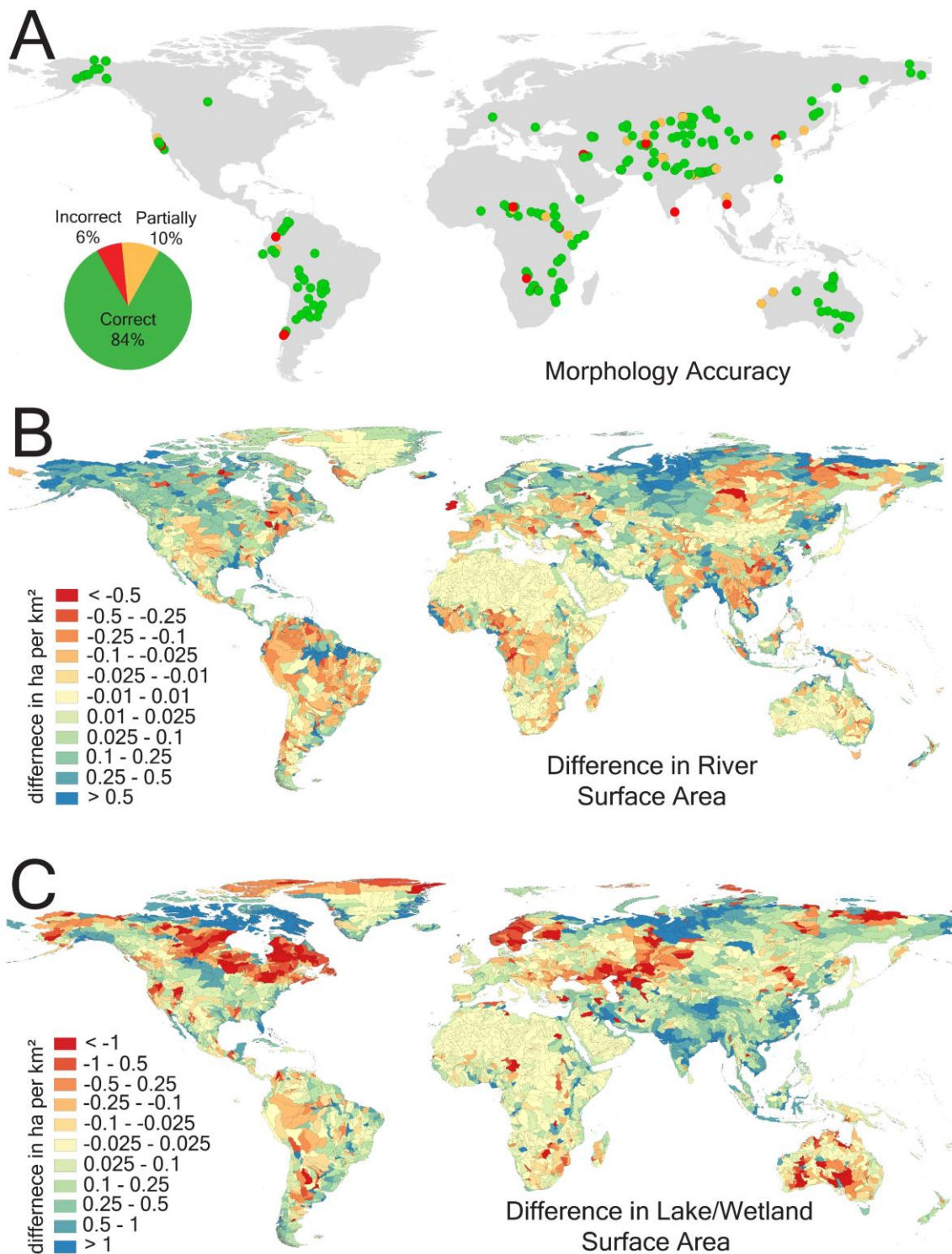


Figure 7 Global River Morphology Accuracy – A) Accuracy of GRM morphology compared to manual classifications by Hartley et al.,¹⁹ B) difference in river surface area per km² within each sub-catchment between the GRM and the GRWL datasets³ and C) difference in wetland/lacustrine surface area per km² within each sub-catchment between the GRM and the HydroLAKES datasets³⁸.

Acknowledgements

We would like to thank Adrian Hartley for kindly providing the locations of the manual interpretations of river morphologies used to compare to the current GRM model. Linling Chen is thanked for reviewing an earlier version of manuscript. Jim Pizzuto and one anonymous reviewer are thanked for their constructive comments. This study was funded by the Architectural Element Characterization of Fluvial Systems project by AkerBP ASA.

Data Availability

The interactive map of the global river morphology (GRM) model is available at bit.ly/3O3GaR0. The data repository is publicly available at [10.5281/zenodo.6624935](https://doi.org/10.5281/zenodo.6624935).

References

1. Death, R. G., Fuller, I. C. & Macklin, M. G. Resetting the river template: the potential for climate-related extreme floods to transform river geomorphology and ecology. *Freshw. Biol.* **60**, 2477–2496 (2015).
2. Ouellet Dallaire, C., Lehner, B., Sayre, R. & Thieme, M. A multidisciplinary framework to derive global river reach classifications at high spatial resolution. *Environ. Res. Lett.* **14**, 24003 (2019).
3. George, A. H. & Tamlin, P. M. Global extent of rivers and streams. *Science (80-.)*. **361**, 585–588 (2018).
4. Oki, T. & Kanae, S. Global Hydrological Cycles and World Water Resources. *Science (80-.)*. **313**, 1068 LP – 1072 (2006).
5. Dottori, F. *et al.* Increased human and economic losses from river flooding with anthropogenic warming. *Nat. Clim. Chang.* **8**, 781–786 (2018).
6. Hirabayashi, Y. *et al.* Global flood risk under climate change. *Nat. Clim. Chang.* **3**, 816–821 (2013).
7. Winsemius, H. C. *et al.* Global drivers of future river flood risk. *Nat. Clim. Chang.* **6**, 381–385 (2016).
8. Fryirs, K. A. River sensitivity: a lost foundation concept in fluvial geomorphology. *Earth Surf. Process. Landforms* **42**, 55–70 (2017).
9. Leopold, L. B. & Wolman, M. G. *River channel patterns: Braided, meandering, and straight. Professional Paper* <http://pubs.er.usgs.gov/publication/pp282B> (1957) doi:10.3133/pp282B.
10. Nanson, G. C. & Croke, J. C. A genetic classification of floodplains. *Geomorphology* **4**, 459–486 (1992).
11. Rinaldi, M., Gurnell, A. M., del Tánago, M. G., Bussetini, M. & Hendriks, D. Classification of river morphology and hydrology to support management and restoration. *Aquat. Sci.* **78**, 17–33 (2016).
12. Schumm, S. A. Patterns of alluvial rivers. *Annu. Rev. Earth Planet. Sci.* **13**, 5–27 (1985).
13. Nanson, G. C. & Knighton, A. D. Anabranching Rivers: Their Cause, Character and Classification. *Earth Surf. Process. Landforms* **21**, 217–239 (1996).

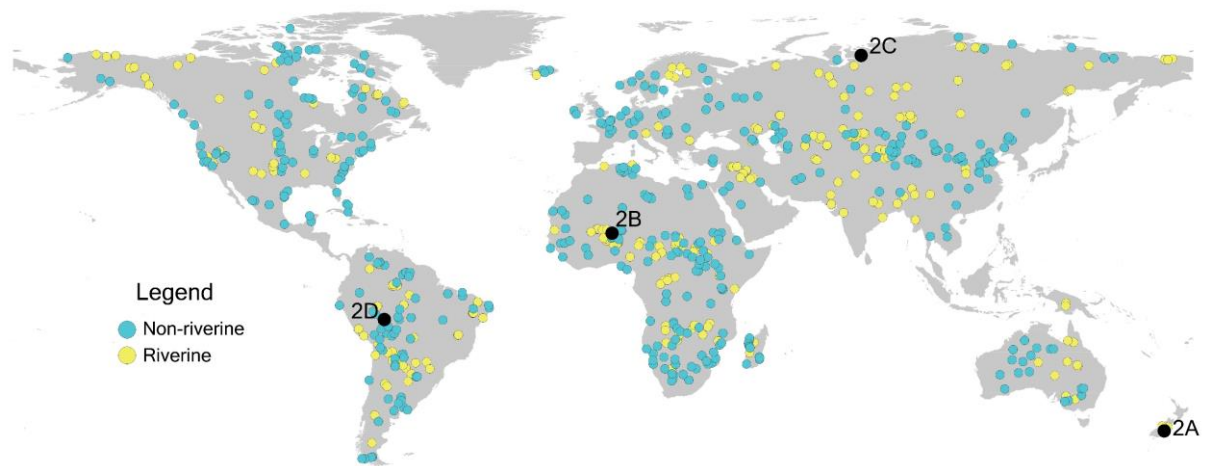
14. Gorelick, N. *et al.* Google Earth Engine: Planetary-scale geospatial analysis for everyone. *Remote Sens. Environ.* **202**, 18–27 (2017).
15. Pekel, J.-F., Cottam, A., Gorelick, N. & Belward, A. S. High-resolution mapping of global surface water and its long-term changes. *Nature* **540**, 418–422 (2016).
16. Tsendbazar, N. *et al.* Towards operational validation of annual global land cover maps. *Remote Sens. Environ.* **266**, 112686 (2021).
17. Brown, C. F. *et al.* Dynamic World, Near real-time global 10 m land use land cover mapping. *Sci. Data* **9**, 251 (2022).
18. Grill, G. *et al.* Mapping the world’s free-flowing rivers. *Nature* **569**, 215–221 (2019).
19. Hartley, A. J., Weissmann, G. S., Nichols, G. J. & Warwick, G. L. Large Distributive Fluvial Systems: Characteristics, Distribution, and Controls on Development. *J. Sediment. Res.* **80**, 167–183 (2010).
20. Davidson, S. K., Hartley, A. J., Weissmann, G. S., Nichols, G. J. & Scuderi, L. A. Geomorphic elements on modern distributive fluvial systems. *Geomorphology* **180–181**, 82–95 (2013).
21. Dong, T. Y. & Goudge, T. A. Quantitative relationships between river and channel-belt planform patterns. *Geology* **50**, 1053–1057 (2022).
22. Feng, D., Gleason, C. J., Yang, X., Allen, G. H. & Pavelsky, T. M. How Have Global River Widths Changed Over Time? *Water Resour. Res.* **58**, e2021WR031712 (2022).
23. Nyberg, B., Gawthorpe, R. L. & Helland-Hansen, W. The distribution of rivers to terrestrial sinks: Implications for sediment routing systems. *Geomorphology* **316**, 1–23 (2018).
24. Hartley, A. J., Owen, A., Weissmann, G. S. & Scuderi, L. Modern and ancient amalgamated sandy meander-belt deposits: recognition and controls on development. (2018).
25. Hansen, M. C., Defries, R. S., Townshend, J. R. G. & Sohlberg, R. Global land cover classification at 1 km spatial resolution using a classification tree approach. *Int. J. Remote Sens.* **21**, 1331–1364 (2000).
26. Lehner, B., Verdin, K. & Jarvis, A. New Global Hydrography Derived From Spaceborne Elevation Data. *Eos, Trans. Am. Geophys. Union* **89**, 93–94 (2008).
27. Rosgen, D. L. A classification of natural rivers. *CATENA* **22**, 169–199 (1994).
28. Hartmann, J. & Moosdorf, N. The new global lithological map database GLiM: A representation of rock properties at the Earth surface. *Geochemistry, Geophys. Geosystems* **13**, Q12004 (2012).
29. Yamazaki, D. *et al.* A high-accuracy map of global terrain elevations. *Geophys. Res. Lett.* **44**, 5844–5853 (2017).
30. Kale, V. S. Geomorphic Effects of Monsoon Floods on Indian Rivers - Flood Problem and Management in South Asia. in (eds. Mirza, M. M. Q., Dixit, A. & Nishat, A.) 65–84 (Springer Netherlands, 2003). doi:10.1007/978-94-017-0137-2_3.
31. Orlandini, S., Moretti, G. & Albertson, J. D. Evidence of an emerging levee failure mechanism causing disastrous floods in Italy. *Water Resour. Res.* **51**, 7995–8011 (2015).

32. Entwistle, N., Heritage, G. & Milan, D. Flood energy dissipation in anabranching channels. *River Res. Appl.* **34**, 709–720 (2018).
33. Matthews, E., Johnson, M. S., Genovese, V., Du, J. & Bastviken, D. Methane emission from high latitude lakes: methane-centric lake classification and satellite-driven annual cycle of emissions. *Sci. Rep.* **10**, 12465 (2020).
34. Drake, T. W., Raymond, P. A. & Spencer, R. G. M. Terrestrial carbon inputs to inland waters: A current synthesis of estimates and uncertainty. *Limnol. Oceanogr. Lett.* **3**, 132–142 (2018).
35. Stets, E. G. *et al.* Carbonate buffering and metabolic controls on carbon dioxide in rivers. *Global Biogeochem. Cycles* **31**, 663–677 (2017).
36. Shorten, C. & Khoshgoftaar, T. M. A survey on Image Data Augmentation for Deep Learning. *J. Big Data* **6**, 60 (2019).
37. Sayre, R. *et al.* A new 30 meter resolution global shoreline vector and associated global islands database for the development of standardized ecological coastal units. *J. Oper. Oceanogr.* **12**, S47–S56 (2019).
38. Messenger, M. L., Lehner, B., Grill, G., Nedeva, I. & Schmitt, O. Estimating the volume and age of water stored in global lakes using a geo-statistical approach. *Nat. Commun.* **7**, 13603 (2016).
39. Simonyan, K. & Zisserman, A. Very deep convolutional networks for large-scale image recognition. *arXiv Prepr. arXiv1409.1556* (2014).
40. Deng, J. *et al.* ImageNet: A large-scale hierarchical image database. in *2009 IEEE Conference on Computer Vision and Pattern Recognition* 248–255 (2009). doi:10.1109/CVPR.2009.5206848.
41. Song, C., Huang, B., Richards, K., Ke, L. & Hien Phan, V. Accelerated lake expansion on the Tibetan Plateau in the 2000s: Induced by glacial melting or other processes? *Water Resour. Res.* **50**, 3170–3186 (2014).

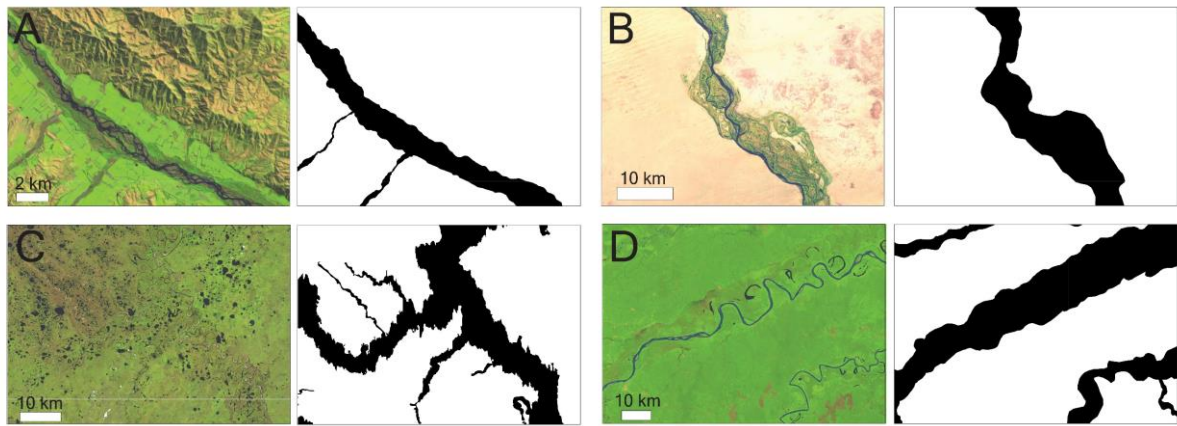
Extended Figures and Tables

Extended Table 1 Riverine and Lacustrine Distribution – The surface area contribution of each environment in km² subdivided by continent. Percentages show the proportion of the total within each category classified as meandering.

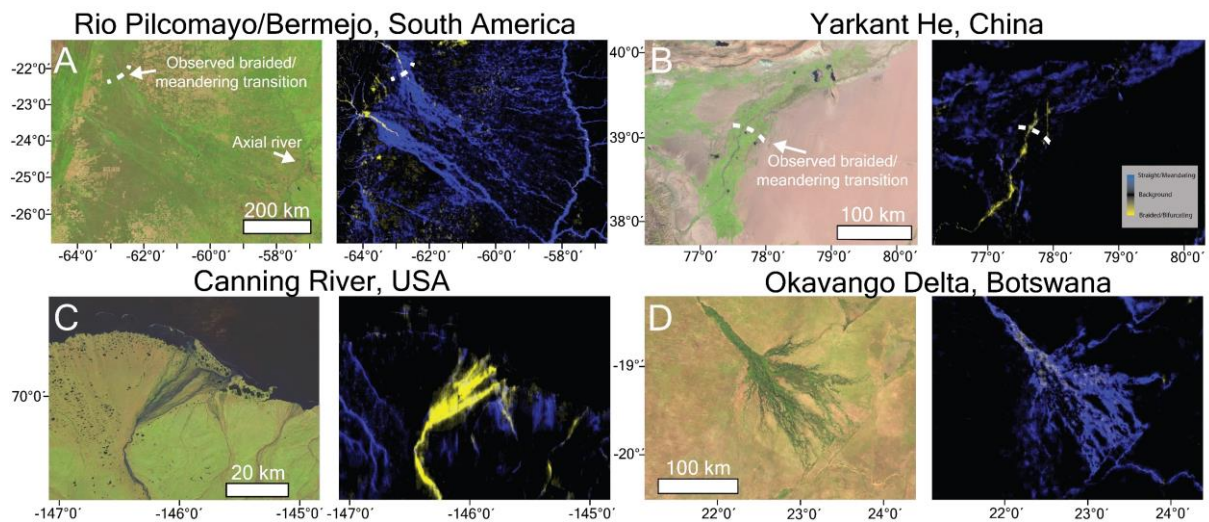
	Abandoned Channel Belt	Active Channel Belt	River	Smaller Lakes or Rivers	Channel Belt Total	Lakes	Total
Africa	2.88x10 ⁵ (86%)	0.26x10 ⁵ (76%)	0.41x10 ⁵ (52%)	0.08x10 ⁵ (64%)	3.62x10 ⁵ (81%)	2.54x10 ⁵	6.16x10 ⁵
Asia	7.23x10 ⁵ (80%)	1.30x10 ⁵ (60%)	2.14x10 ⁵ (44%)	0.68x10 ⁵ (71%)	11.35x10 ⁵ (71%)	9.73x10 ⁵	21.1x10 ⁵
Europe	1.3x10 ⁵ (77%)	0.19x10 ⁵ (60%)	0.34x10 ⁵ (43%)	0.18x10 ⁵ (54%)	2.04x10 ⁵ (68%)	2.78x10 ⁵	4.82x10 ⁵
Oceania	1.6x10 ⁵ (87%)	0.14x10 ⁵ (83%)	0.06x10 ³ (63%)	0.02x10 ⁵ (79%)	1.82x10 ⁵ (86%)	0.28x10 ⁵	2.10x10 ⁵
North America	2.9x10 ⁵ (85%)	0.26x10 ⁵ (72%)	0.79x10 ⁵ (53%)	0.36x10 ⁵ (75%)	4.34x10 ⁵ (78%)	13.8x10 ⁵	18.1x10 ⁵
South America	5.7x10 ⁵ (9%)	0.56x10 ⁵ (83%)	0.98x10 ⁵ (52%)	0.15x10 ⁵ (72%)	7.36x10 ⁵ (85%)	1.55x10 ⁵	8.91x10 ⁵
Total	22.7x10 ⁵ (85%)	2.70x10 ⁵ (69%)	4.72x10 ⁵ (48%)	1.46x10 ⁵ (70%)	30.5x10 ⁵ (77%)	30.6x10 ⁵	61.2x10 ⁵



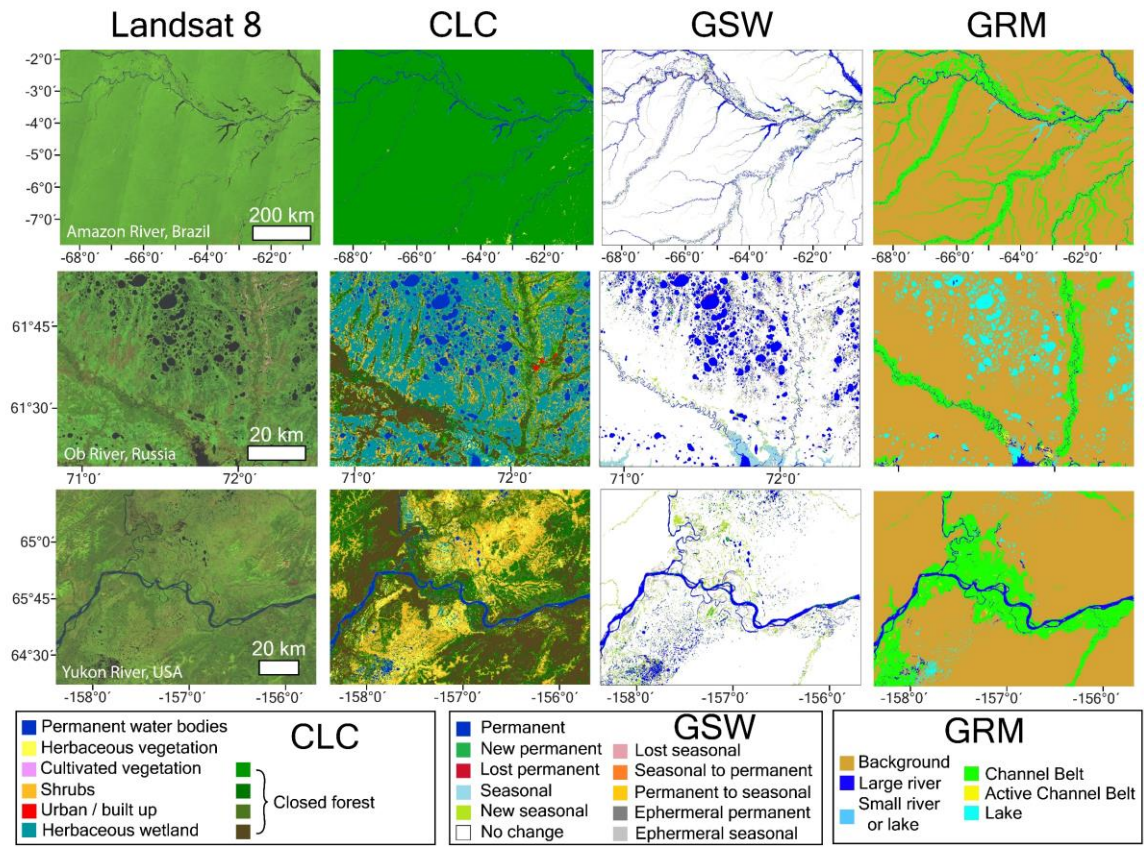
Extended Figure 1 Global River Morphology Training Locations – Global distribution of riverine and non-riverine locations used to train and validate the machine learning algorithm. Overlain numbers refer to the examples shown in the Extended Figure 2.



Extended Figure 2 Global River Morphology Training Examples – Typical examples of training images used in the GRM machine learning algorithm showing the original image and the mask containing a classification of either meandering or braided.



Extended Figure 3 Global River Morphology Prediction Examples – Examples of the GRM prediction for different river systems covering a range of climates and tectonic settings. The observed braided to meandering transition in A and B are based on descriptions and illustrations previously reported by Hartley et al.¹⁹ and Davidson et al.²⁰



Extended Figure 4 Global Riverine and Lacustrine Environment Examples – Comparison of different global land and water classifications of the Copernicus Land Cover (CLC) Map¹⁶, Global Surface Water (GSW) Map¹⁵ and the Global River Morphology (GRM) map.